Gold Nanoparticles for CO$_2$ Electroreduction: An Optimum Defined by Size and Shape

Esperanza Sedano Varo,[∥] Rikke Egeberg Tankard,[∥] Joakim Kryger-Baggesen, Joerg Jinschek, Stig Helveg, Ib Chorkendorff, Christian Danvad Damsgaard, and Jakob Kibsgaard[*]

ACCESS | Metrics & More | Article Recommendations | Supporting Information

ABSTRACT: Understanding the size-dependent behavior of nanoparticles is crucial for optimizing catalytic performance. We investigate the differences in selectivity of size-selected gold nanoparticles for CO$_2$ electroreduction with sizes ranging from 1.5 to 6.5 nm. Our findings reveal an optimal size of approximately 3 nm that maximizes selectivity toward CO, exhibiting up to 60% Faradaic efficiency at low potentials. High-resolution transmission electron microscopy reveals different shapes for the particles and suggests that multiply twinned nanoparticles are favorable for CO$_2$ reduction to CO. Our analysis shows that twin boundaries pin 8-fold coordinated surface sites and in turn suggests that a variation of size and shape to optimize the abundance of 8-fold coordinated sites is a viable path for optimizing the CO$_2$ electrocatalytic reduction to CO. This work contributes to the advancement of nanocatalyst design for achieving tunable selectivity for CO$_2$ conversion into valuable products.
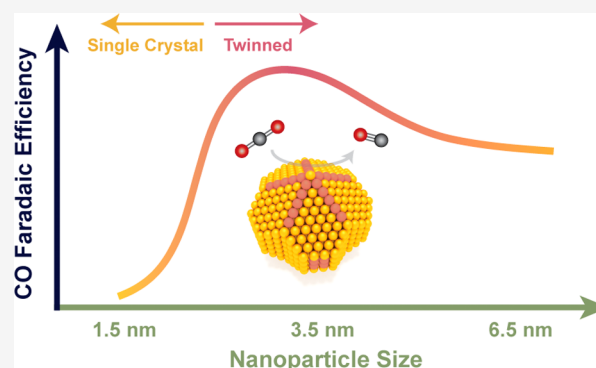
INTRODUCTION

The continued increase in atmospheric carbon dioxide (CO$_2$) levels, largely caused by human activity, has become a pressing global concern due to its negative impact on the environment and climate. To mitigate the effects of climate change, there is a need to develop effective methods for the reduction of CO$_2$ into valuable chemicals that can be used as fuels or feedstocks for various industrial processes.[1,2] The CO$_2$ electroreduction field is shifting into a two-step solution, where CO$_2$ is first reduced to CO, and then CO is transformed into the product of interest. The development of industrially relevant applications of electrochemical CO$_2$ reduction relies on an improvement in the catalyst structure to enhance the efficiency and selectivity for the desired reaction for both the first and second steps.

Gold (Au) is one of the most selective catalysts for electrochemical reduction of CO$_2$ to CO, albeit there is a selectivity challenge toward the ever-competing hydrogen evolution reaction (HER). Nanoparticles (NPs) provide a unique possibility for tuning catalytic performance, with electronic properties that can vary significantly with only small changes in the NP diameter and structure.[3−5] Due to their high surface area-to-volume ratio, NPs allow for an efficient use of the catalyst material,[6,7] and the ability to modify their surface structure can enable control over the reaction pathway and products formed. Specifically, this control relies on managing the relative distribution of distinct active sites and may be achieved by manipulating parameters such as size,

shape, and composition.[8,9] However, a rational optimization requires an atomically resolved surface site distribution to obtain a structure−activity relationship.

The size of Au NPs has previously been found to play an important role in their catalytic activity for CO$_2$ electroreduction. Zhu *et al.*[10] calculated the density of adsorption sites on closed-shell cuboctahedral Au clusters of different sizes. Their theoretical findings indicate an optimal size range for CO formation of 2.7−4 nm, attributed to a high density of edge sites. Additionally, Mistry *et al.*[11] demonstrated that Au NPs exhibited high activities for CO$_2$ electroreduction compared to bulk Au and suggested that coverage of CO and H could play a role in size-dependent trends. The authors observed that NPs below 2 nm had an increased overall activity, explained by a higher density of low-coordinated sites. However, the shape of Au NPs is not linearly scalable with their size because multiple twinned particles can form above a size threshold[12,13] and thus affect the distribution of specific surface sites in a way that is difficult to predict. Here, we uncover the relation between electrocatalytic reduction of CO$_2$ and abundance of surface sites on size-selected Au NPs by
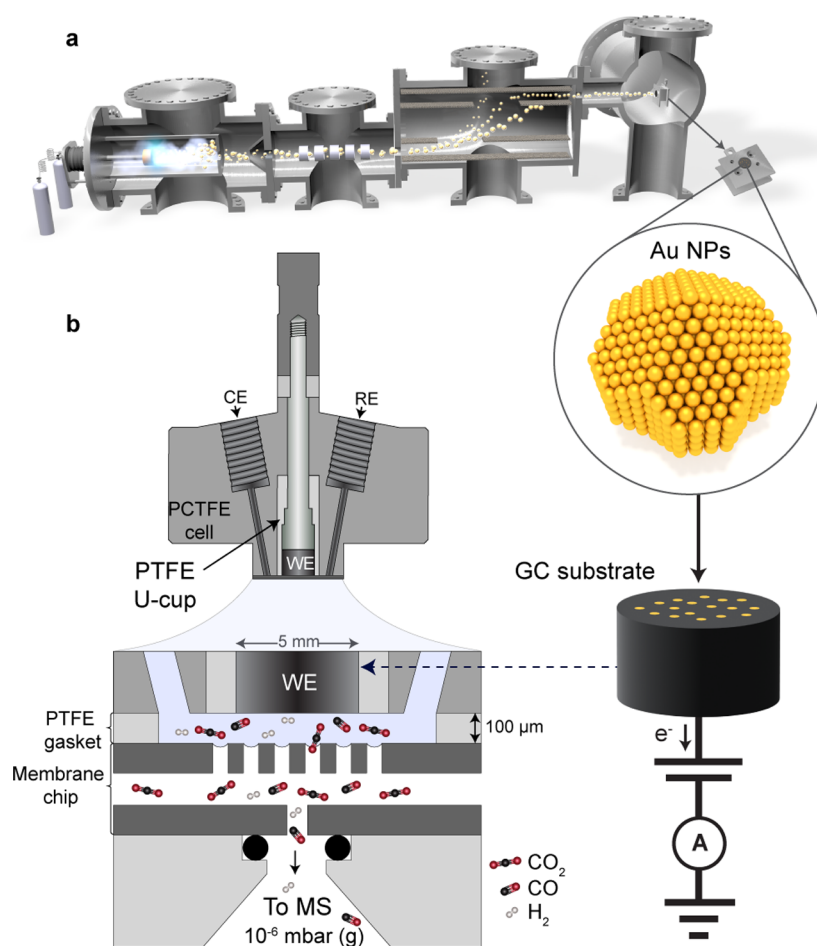
Figure 1. Preparation and testing of the Au NPs. (a) Schematic of the UHV Nanobeam 2011 cluster source (Birmingham Instruments, Ltd.) used for the synthesis of the NPs. The illustration shows how the loading of NPs is monitored by detecting a neutralization current as the charged NPs impinge onto the GC sample. (b) The electrochemical cell used for testing the activity of the samples allows for high-sensitivity detection of products.[13] Colors for ball models: red = oxygen, black = carbon, and white = hydrogen.

introducing highly sensitive electrocatalytic activity measurements of small loadings of Au NPs and estimating surface site distributions based on atomically resolved electron micrographs of the Au NPs.

We produced 5 different Au NP sizes between 1.5 and 6.5 nm (based on an initial spherical approximation) using a magnetron-based cluster source. This size range covers the transition from clusters to NPs[4], but for a better flow of reading, they are all referred to as NPs in the following text. We deposited the NPs onto mirror-polished glassy carbon (GC) substrates and tested their activity for CO_2 electro-reduction. The process for the synthesis and electrochemical testing of the samples is outlined in Figure 1.

Figure 1a shows a schematic of the cluster source in which the NPs were produced using magnetron sputtering followed by gas-phase aggregation and size selection by a time-of-flight filter.[14] This method allows for a narrow size distribution with a resolution of $m/\Delta m = 20$, as well as achieving homogeneously dispersed NPs on the entire electrode surface. Before deposition, the GC substrates were cleaned by Ar^+ sputtering and analyzed for impurities with ion scattering spectroscopy (ISS). The loading of Au NPs on each sample was chosen to be equivalent to a projected area coverage of 5% of the surface. The coverage is a compromise between being large enough for a decent signal for electrochemical testing yet

small enough to minimize sintering of the NPs on the surface. The loading of NPs was detected by measuring the neutralization current resulting from the charged NPs impinging on the substrate, and they were uniformly dispersed by rastering the substrate in front of the deposition beam. The accurate counting of the NPs hitting the surface of the electrode combined with the narrow size distribution of the deposition allows a precise normalization of the electrochemically active surface area (ECSA). We tested the samples in a chip-interfaced EC–MS (electrochemistry–mass spectrometry) setup (shown in Figure 1b), allowing for a high-sensitivity and real-time detection of the products.[15]

We verified the homogeneity of the NP distribution as well as their sizes using scanning electron microscopy (SEM) and atomic force microscopy (AFM) directly on the GCs which were used for electrochemistry. Three sizes of interest based on the catalytic data were also deposited on graphene-covered transmission electron microscopy (TEM) grids to mimic the GC surface. The atomically resolved TEM data indicate a trend in the NP shape for different NP sizes, which can help explain the differences observed in catalytic performance. With the narrow size resolution of the cluster source mass selection method, we uncovered a convoluted electrocatalytic optimum consistent with previous theoretical studies,[10,16] which can be rationalized based on the characterization data presented.
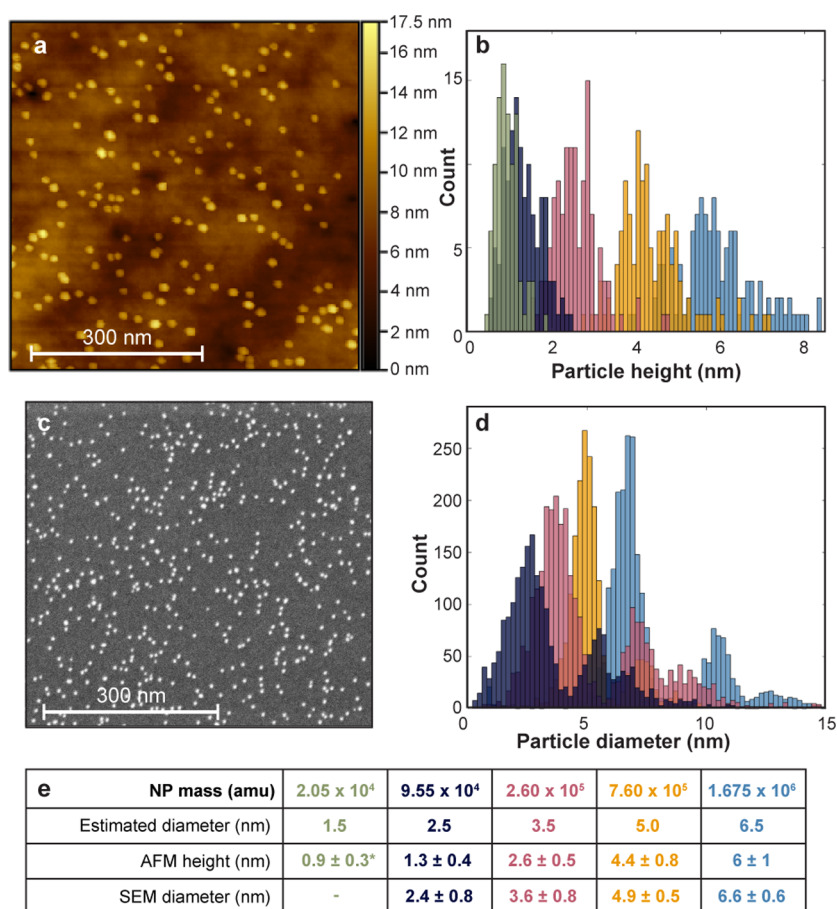
Figure 2. AFM and SEM data for the 5 different Au NP sizes. (a) Example AFM image of a GC with 6.5 nm NPs. (b) Height measurements from tapping-mode AFM in air on the GC substrates. *The 1.5 nm NPs were too small to be resolved on the GC, so the height data for these NPs are instead from AFM measurements on a TEM grid, where the flatter graphene substrate made it possible to resolve the particles. (c) Example SEM image of a GC with 3.5 nm NPs. (d) Measured NP diameters from SEM images. A comparison between the expected NP diameter based on a spherical approximation, the measured NP heights in AFM, and the NP diameters from SEM is given in (e). The discrepancies between the techniques highlights the challenges with estimating the NP sizes from one method only.

e NP mass (amu)	2.05×10^4	9.55×10^4	2.60×10^5	7.60×10^5	1.675×10^6
Estimated diameter (nm)	1.5	2.5	3.5	5.0	6.5
AFM height (nm)	0.9 ± 0.3*	1.3 ± 0.4	2.6 ± 0.5	4.4 ± 0.8	6 ± 1
SEM diameter (nm)	-	2.4 ± 0.8	3.6 ± 0.8	4.9 ± 0.5	6.6 ± 0.6

■ RESULTS

Nanoparticle Sizes. Au NPs of masses 20.5k amu, 95.5k amu, 260k amu, 760k amu, and 1.675 M amu were selected in the cluster source. As a first approximation, we assume that the NPs are spherical and metallic and use the density of Au of 19.32 g/cm^3, giving corresponding estimated diameters of the NPs of 1.5, 2.5, 3.5, 5.0, and 6.5 nm. However, it is known that especially for smaller NPs, a spherical approximation is inaccurate and the real size depends on the detailed shape of the NP.[17]

Typically, in experimental studies of activity *vs* NP size, microscopy techniques are used to determine the size of the NPs. The description of the NP size from microscopy measurements (and any assumptions regarding the shape) is important when one wants to link activity behavior to the NP size and shape. Here, we measured the heights and diameters of the NPs directly on the GC substrates using tapping-mode AFM and SEM. The results are displayed in Figure 2. The graphs in Figure 2b,d show the distributions of the heights and diameters of the NPs from AFM and SEM, respectively. The obtained values for each sample are summarized in Figure 2e along with the estimated diameters.

The data from AFM and SEM provide different types of information about the NPs. We used tapping-mode AFM in air

on the GCs to measure the topographic heights of the NPs. An example AFM image of a GC surface with 6.5 nm NPs is shown in Figure 2a. The underlying roughness of the GC (measured rms = 3.0 nm with AFM on a blank GC) is visible as well as the NPs. For the smaller NPs, the roughness of the substrate relative to the NP heights caused the height measurements to be underestimated. The smallest NPs (of an estimated diameter 1.5 nm) were not possible to resolve on the GCs but could be resolved on the graphene-covered TEM grids due to the smaller roughness of graphene. To mitigate influences on the height measurements by tip shape,[18,19] we scanned the same sample with several different tips (see further details in Section S.2 of the Supporting Information). When treating the data, care was taken to avoid using averaging processing techniques on the GC background as this caused a shift in the size measured to lower sizes due to the significant roughness. The full image treatment process is given in Section S.2 in the Supporting Information along with more images and further details on the data treatment from AFM. The height information (in *z*) from AFM is only a complementary measurement in determining the NP sizes, and care should be taken not to quote the height directly as the NP diameter as this can be misleading. The "width" of NPs with sizes <6.5 nm in the *xy* plane is generally not possible to determine using this type of AFM as the lateral size will appear larger due to
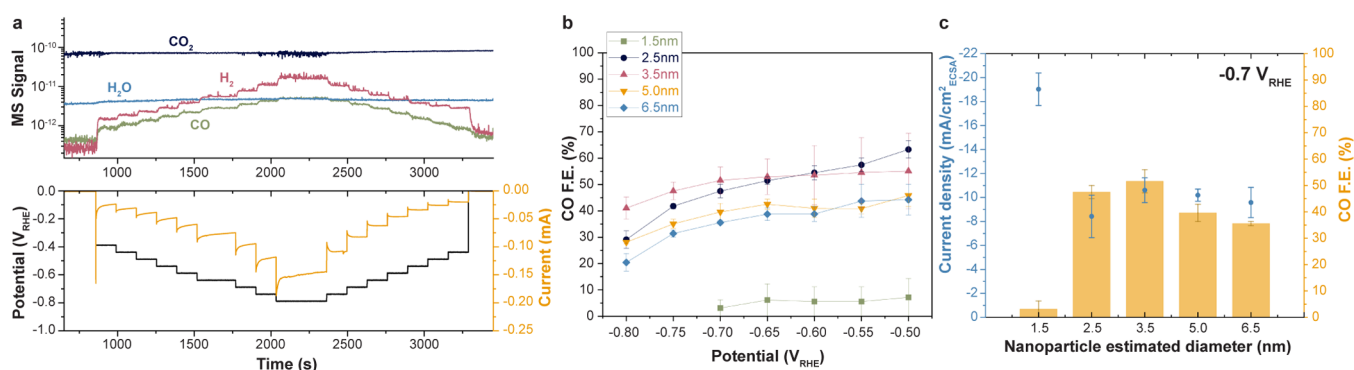
Figure 3. Electrochemical performance of the size-selected Au NPs. (a) Example of electrochemical "staircase" experiment performed with the NPs, in this case for a 3.5 nm sample. (b) CO FE for each size depending on the applied potential. (c) FE toward CO at -0.7 V_{RHE} and the total current density (Au ECSA) for each size.

influences of lateral forces on the tip, and the tip radius ($\sim$10 nm) poses severe limitations.

SEM images before electrochemistry were used to verify the homogeneity of deposition across the sample and to obtain an approximate size distribution of the NPs. An example SEM image of 3.5 nm NPs is shown in Figure 2c. At least one sample of each size of the selected NPs was investigated by SEM imaging, except for the smallest size, which could not be resolved in SEM. The NPs were evenly distributed in all GC samples across different parts of the sample. The obtained size distributions are shown in Figure 2d, and for each size, we observed a second peak at a larger size corresponding to NPs with double mass/double charge that also pass through the mass filter. We saught to suppress these before deposition by shifting the maximum of the mass distribution spectrum in the cluster source toward smaller sizes than the desired NP mass. SEM provides information about size distribution, but manual adjustments to parameters such as threshold and contrast can be potential sources of error when extracting such information from microscopy images. For example, when extracting data from SEM images, the measured size distribution seems larger for smaller NPs when compared to the AFM data, which can be explained by the low signal-to-noise ratio in these SEM images. Therefore, we used the SEM images as a verification and not as a definition technique to state the size distribution in our samples.

Our results demonstrate that using complementary techniques is important when analyzing the size and the homogeneity in the dispersion of the NPs, and we highlight that the complexity of the measurement techniques needs to be considered both for the data acquisition and analysis procedure and in how the data are presented. The SEM and AFM data show the uniformity of the NP deposition directly on the substrates used for electrochemical measurements, and they provide good evidence for an even difference in the sizes of the NPs produced. However, both techniques are limited in resolution and therefore do not provide atomically resolved information about the NPs. Hence, in order to truly understand the NP structure (and "size"), atomic resolution is necessary, and we present such data using high-resolution TEM (HRTEM) in the following.

Activity and Selectivity. We measured the activity of the samples in a 3-electrode electrochemical cell coupled to a mass spectrometer through a chip, which limits the flow of molecules through a microcapillary. As shown in Figure 3a, the electrochemical protocol consisted of introducing the

samples under potential control and then ramping the potential by steps of -50 mV and measuring the current response. The mass spectrometer detected the products (H_2 and CO) in real time, allowing for a continuous product analysis at each potential. The results of the performance for CO_2 electroreduction show that the Faradaic efficiency (FE) toward CO varies depending on the size of the NPs, as highlighted in Figure 3b,c. Depending on their behavior, as observed in Figure 3b, we classify the samples into three distinct groups: the 2.5 and 3.5 nm samples present the best CO activity and selectivity at every potential; the 5.5 and 6.5 nm samples are more selective toward H_2, decreasing the production of CO; and the 1.5 nm sample shows a completely different behavior, producing almost exclusively H_2. As an overall trend, the selectivity toward CO is higher at less negative potentials, for all the sizes studied. The optimum size at low overpotential is found to be 2.5 nm, reaching up to 63% FE toward CO at -0.5 V_{RHE}, closely followed by the performance observed for the 3.5 nm sample. The 1.5 nm samples mainly produced H_2 as result of the competitive HER reaction taking over CO_2 electroreduction, exhibiting the worst performance among all the samples. The larger sizes (5 and 6.5 nm) were substantially less selective toward CO, having a FE toward CO 15−20% lower than that of the 2.5−3.5 nm samples at the same potentials. Interestingly, current densities were found to be similar within the error for all sizes from 2.5 nm and above, indicating a similar ECSA, since the current is dominated by the deposited NPs. The background current from the blank GCs is shown in the Supporting Information, Figure S9. However, the current density for the 1.5 nm samples was higher, as seen in Figure 3c, which can be explained by a higher activity toward the HER.[11,20]

We have observed that controlling the coverage of NPs is crucial to draw accurate conclusions about their selectivity, as discussed in Figure S6 of the Supporting Information. For example, for the 5 nm sample, a lower loading is more selective toward H_2 and counterintuitively has a higher current response, even if the ECSA is approximately half of the original sample. This could be attributed to the difference in the interparticle distance, which would influence the local pH, the diffusion of reactants and products, and the stabilization of intermediates.[21−23] Therefore, we chose to keep the coverage constant at 5% of the projected area of the electrode, low enough to minimize sintering of the neighboring NPs but high enough to get a good signal from the products. In addition, we have found that the cleanliness of the GC plays a fundamental
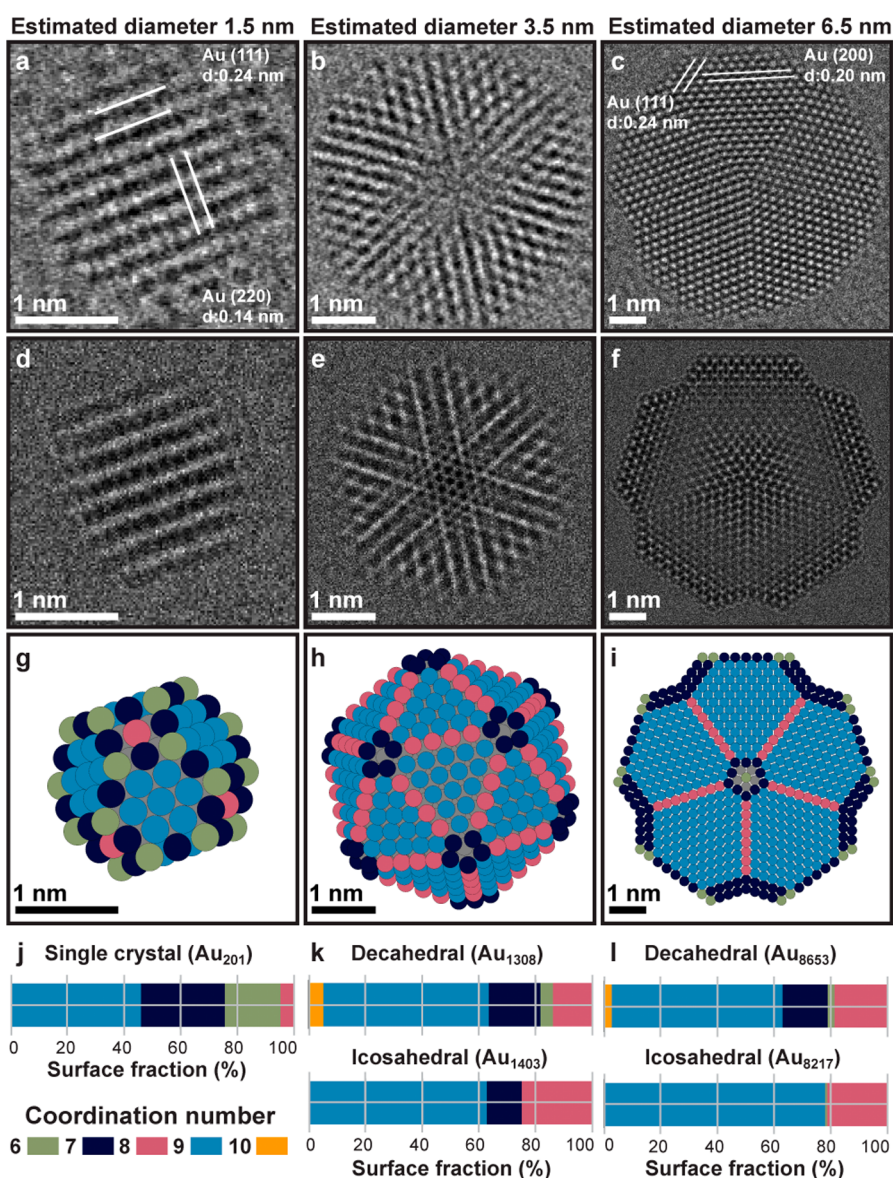
Figure 4. Structural investigation of NP surface structures. (a−c) HRTEM images of single Au NPs with estimated diameters of 1.5, 3.5, and 6.5 nm, respectively. Notice that the HRTEM image of the 1.5 nm NP reflects a single crystal, and the images of the 3.5 and 6.5 nm reveal an MTP structure. (d−f) Simulated HRTEM images of a 1.5 nm single crystal (g), 3.5 nm icosahedral (h), and 6.5 nm decahedral (i) NP structure, respectively (see the Materials and Methods section for details). The three-dimensional structure models used in (g−i) have the surface atoms colored according to the coordination number (bulk atoms are colored gray). In (j−l), the fraction of surface sites according to the coordination of the structure models is shown.

role in the selectivity of the NPs. Our samples have a small loading (between 100 and 400 ng/cm^2), and therefore, most of the GC area is not covered by the NPs. Thus, impurities on the support can significantly influence the activity and selectivity. Consequently, we took extreme care in the cleaning procedure of the GCs and meticulously analyzed the surface of the GCs with ISS before deposition. We observed that some GCs contained high levels of intrinsic contamination (>2000 counts), which could not be removed using Ar$^+$ sputtering, and at these levels, an increased production of H$_2$ was observed in EC measurements, as shown in Figure S8 in the Supporting Information. Therefore, we selected only GCs with lower contamination levels that exhibited a negligible H$_2$ production in the EC measurements.

Characterization of Surface Sites. To investigate the relationship between the catalytic properties and the atomic

structure, we acquired HRTEM images of NPs with nominal sizes of 1.5, 3.5, and 6.5 nm deposited on graphene-covered Au grids. Representative images of single NPs are shown in Figure 4a−c respectively (see the Materials and Methods section for experimental details). These particular sizes were chosen as they represent the lower, top, and higher limits of the activity plateau seen in Figure 3c. For each of the three samples, images of 30 particles were acquired as in their as-prepared state. For the 1.5 nm sample, HRTEM images reveal that the majority (24/30) of the NPs had atomic lattice fringes with spacings and orientations consistent with single crystalline Au, as depicted in Figures 4a and S11 in the Supporting Information. For the 3.5 and 6.5 nm, HRTEM images of all the observed NPs (30/30) reveal lattice fringes consistent with polycrystalline Au in the shape of multiply twinned particles (MTPs). No particles with a single crystal shape were observed

for these larger sizes. These two-dimensional projected shapes are attributed to decahedral and icosahedral shapes, consistent with earlier reports.[12,13,24] Both shapes were observed among the 3.5 and 6.5 nm wide NPs, although only one of each is shown in Figure 4b,c.

To investigate whether the MTP structures were still present after electrocatalytic measurements, HRTEM images were also acquired post-mortem of samples loaded with 3.5 and 6.5 nm Au NPs following the same protocol as that applied for Figure 3a. In total, HRTEM images were acquired of 17 NPs on the electrochemically tested samples (5 for the 3.5 nm sample and 12 for the 6.5 nm sample). Figure S10 in the Supporting Information shows representative images of NPs for both samples. The images and their corresponding fast Fourier transform (FFT) reflect NPs with sizes roughly corresponding the as-prepared states and with atomic lattice fringes reflecting MTP structures. That the MTP structures appear after the electrocatalysis is indicative of the fact that the reaction conditions were sufficiently mild to only perturb the surface site distribution to a minor degree, as depicted for instance in Figure S10b. Thus, the proposed structures of the as-prepared NP will now be addressed to access the surface site distributions.

To rationalize the two-dimensional Au NP shapes in Figure 4a–c with a three-dimensional structure model, we consider a Wulff constructed model.[25] The Wulff[25] model yields an equilibrium shape based on known surface energies. While the Wulff[25] construction commonly assumes a single crystal object, Marks[26] included twin boundary energies in what is known as the Modified Wulff[26] construction, explaining the stability of MTPs in particular decahedral and icosahedral shapes. Following Marks'[26] approach, we construct three-dimensional structure models of NPs with estimated diameters of 1.5, 3.5 and 6.5 nm, using the known Au surface and twin boundary energies.[27,28] The structural models are oriented according to the zone axis orientation in the corresponding HRTEM images in Figure 4a–c (see Figure S11 in the Supporting Information), and subsequently, HRTEM images are simulated under optical conditions matching the experimental observations (see the Materials and Methods section). Figure 4d–f resemble visually Figure 4a–c. Thus, the structural models in Figure 4g–i are approximating the NP structures, although the Au–C interface is likely to truncate the NPs in a plane orthogonal to the electron beam. Based on the approximate unsupported Au NP shapes in Figure 4g–i, the corresponding surface site distributions are quantified for the single crystal, decahedral, and icosahedral shapes in Figure 4j–l.

The quantification in Figure 4j–l shows a clear distinction between the surface site distributions of the single crystal (1.5 nm) and the MTP NPs (3.5 and 6.5 nm). Specifically, the fraction of 8-coordinated surface sites is higher for the MTPs than for the 1.5 nm NP. For the MTPs, the 8-coordinated surface sites correspond to surface terminations of grain boundaries. Previous results have shown that grain boundary sites favor CO_2 reduction,[29] but insights into surface size distribution remain to be determined. Hence, this higher fraction of 8-coordinated sites could explain why the 3.5 and 6.5 nm NPs are more active than the 1.5 nm NP toward CO_2 reduction, as depicted in Figure 3c. Inspection of Figure 4j reveals that the 1.5 nm NP sample has a higher fraction of the 6-(green) and 7-(dark blue) coordinated sites. These sites are known to favor H_2 evolution,[10] further suggesting why the 1.5 nm NP has a lower selectivity toward CO_2 reduction than the

3.5 and 6.5 nm NP. Comparison of Figure 4k,l reveals that the fraction of 9-coordinated (light blue) sites is larger for the 6.5 nm NP than for the 3.5 nm NP, in both the decahedral and icosahedral shape cases. The 9-coordinated (111)-facets are known to favor H_2 evolution,[10] revealing a possible explanation as to why the catalytic activity toward CO_2 reductions is higher for the 3.5 nm NPs than for the 6.5 nm NPs. For larger NPs, the surface fraction of 8-coordinated sites decreases due to a larger fraction of the 9-coordinated sited (111) facet, and thus, a reduced CO_2 reduction activity would be expected with increasing size. It cannot be excluded that the tiny fraction of 10-fold coordinated sites play a role too, since they are present on the 3.5 and 6.5 nm Au NPs too, and would thus be a hitherto unexpected contribution.

Nevertheless, the existence of MTP structures for the 3.5 and 6.5 nm Au NPs, as well as their absence for the 1.5 nm Au NPs, indicates that the MTPs are favorable toward CO_2 reduction. This demonstrates that polycrystallinity evolves with size and stabilizes an enhanced abundance of catalytically important surface sites beyond predictions made by simple Wulff[25] constructions.

◼ CONCLUSIONS

In this study, we investigated the size-dependent behavior of Au NPs ranging from 1.5 to 6.5 nm (estimated diameters) for CO_2 electroreduction. Our findings revealed an optimum size of around 3 nm that maximizes the selectivity toward CO, with ∼60% FE toward CO at low potentials. The determined optimum size is in correspondence with the theoretical prediction from Zhu *et al.* between 2.7 and 4 nm,[10] bearing in mind that this prediction is based on a single crystal model.

Across all studied potentials (ranging from −0.4 to −0.8 V_{RHE}), the 2.5 and 3.5 nm samples demonstrated the highest CO selectivity, displaying a difference of over 15% compared to the 5 and 6.5 nm samples. Interestingly, the smallest size-selected samples (1.5 nm) predominantly produced H_2, potentially attributed to their single crystal structure. The observed trend is different from those reported in previous studies,[10,11] which is attributed to a difference in the NP size control and loading, which may have overshadowed underlying effects due to the size and shape of the NPs.

HRTEM imaging revealed that the shape of the Au NPs varied significantly with the size and that NPs close to the optimal size were the smallest with observed MTP structure. This suggests that MTPs expose surface sites favorable for CO selectivity. Exactly what kind of sites favor CO selectivity is debatable, but previous results show that the grain boundary site density is linearly correlated with the CO_2 activity.[29] We report a surface site analysis showing that the fraction of surface grain boundary sites is the highest for the 3.5 nm MTPs, compared to the 1.5 nm single crystals and 6.5 nm MTPs, supporting the observed activity optimum.

Indeed, the specific shape of the NPs plays an important role in the catalytic properties as well as their size. In other words, to compare the results from different NP sizes, details about the NP shape, which can depend on the synthesis method,[30−32] are crucial. This is valid for electrocatalytic studies as this one but can also have profound implications for thermochemical reactions, where the size of Au NPs has also been found to play a critical role.[16,33−36] Furthermore, we have highlighted the importance of well-controlled, uniform coverages and minimizing the contamination levels in the support. Typical methods used for measuring the NP sizes (such as

AFM, SEM, and TEM) must be used with care and reported with appropriate information about the data treatment procedure. Often these techniques are used solely for determining NP sizes, and simplified assumptions are made about the NP shapes. We underline that such approximations can lead to misinterpretation of the activity data, and new advancements in NP design for optimizing, *e.g.*, selectivity depend on accurate characterization of the shape. Synthesizing Au MTPs with a high grain boundary density is a promising strategy for optimizing nanocatalyst design for CO_2 electro-reduction.

■ MATERIALS AND METHODS

Preparation of GC Substrates. The GC electrodes purchased from MaTecK GmbH (as they were found to contain a minimum amount of intrinsic contaminations) were mirror polished on the deposition side. The physical cleaning consisted of polishing them on a microcloth, first with a 1/4 μm diamond paste and then with a smaller 0.04 μm silica dispersion, to reduce their roughness as much as possible. After this, we immersed the GCs in ultrapure concentrated nitric acid (Suprapur, Supelco) for 1 h as it was found to stabilize the NPs by creating a small roughness observed with AFM. Finally, we rinsed and sonicated the electrodes in ultrapure water and ethanol at least 3 times. The GCs were loaded into the UHV chamber and cleaned by sputtering with Ar$^+$ for 30 min (ion gun settings: 1 keV acceleration voltage, 10 mA emission current, Ar pressure 5×10^{-6} mbar).

Deposition of Nanoparticles. The mass selected Au clusters (20.5k amu, 95.5k amu, 260k amu, 760k amu, and 1.675 M amu) were produced and deposited on the GC substrates and TEM grids using an Ultra-High Vacuum Nanobeam 2011 cluster source (Birmingham Instruments, Ltd.), based on the design of Pratontep *et al.*[37] The instrument works by magnetron sputtering of a Au metal target (99.99% purity), followed by NP growth in a gas-phase aggregation zone with He and Ar gases. The NPs are drawn out of the aggregation zone by the pressure gradient to the adjacent chamber, following which they undergo supersonic expansion and are then filtered by cluster mass (mass-to-charge ratio) in a lateral time-of-flight mass filter[14] before deposition onto the substrate. We note that particles with double mass and double charge also pass through the mass filter, as is shown in Figure 2d. We attempted to minimize these by shifting the mass distribution toward lower mass values before deposition. A potential was applied to the substrate, ensuring soft landing of the NPs[38] (landing energies in the range 0.006−0.462 eV/atom). To ensure a uniform coverage of NPs on the substrate, the sample was rastered in front of the beam using a preset rastering pattern where the beam covers an effective area larger than the 20 mm^2 area of the sample, which has a diameter of 5 mm.

Electrochemical Activity Tests. The 0.1 M KHCO$_3$ electrolyte was prepared using 1.73 g of 99.995% pure K$_2$CO$_3$ (Sigma-Aldrich), dissolving it in 250 mL ultrapure water (Milli-Q, 18.2 MΩ cm), and bubbling the solution with CO$_2$ for at least 30 min until the pH of the solution was 6.8. All electrochemical experiments were performed with a stagnant thin-layer electrochemical cell interfaced with a mass spectrometer[15] through a microporous aqueous chip provided by Spectro Inlets ApS. To remove trace amounts of metal impurities before the experiments, the electrochemical cell was cleaned with Aqua Regia for 3 h and boiled in ultrapure water 3 times for at least 2 h. The spectrometer used for product detection was a QMG250 PRISMAPRO (Pfeiffer A/S), with a selective ionization of 22 eV to avoid splitting of the CO$_2$ (carrier gas) into CO and therefore limiting the background of the 28 amu signal. The electrochemical potential and the current were controlled using a BioLogic SP-150 potentiostat. The EC−MS data were coordinated using ixdat.[39]

The same electrochemical protocol was used for all the samples, except for the smallest NPs, which were unable to reach the same cathodic potential because of the higher current due to H$_2$ production, creating a lot of bubbles and overload on the counter electrode. All the samples were introduced under potential control to minimize their dissolution or mobility,[40] and after applying a slightly negative current (−0.015 mA) for 15 min to reduce surface species and stabilize the mass spectrometer signals, a potential ramping "staircase" experiment was performed. We ramped the potential up and down by steps of 50 mV for 2 min, from −0.4 V$_{RHE}$ to −0.8 V$_{RHE}$ (maintained for 5 min) for most of the samples, except the smallest sizes, which could only reach −0.7 V$_{RHE}$. The ECSA was calculated based on the surface coverage of the sample from the cluster source assuming spherical NPs, which was between 4 and 5% projected coverage.

All the measurements were repeated between 2 and 3 times, and the calibration parameters used for the mass spectrometer signal were very similar for all the samples as the baselines for the H$_2$ and CO signals were very stable over time. The calibration factor for the H$_2$ signal was approximately 0.04 based on internal calibration, calculated by 3 steps of very low currents to have 100% H$_2$ FE.[41] In the case of the CO FE, the calibration factor was approximately 0.014, calculated based on the assumption that Au produces only H$_2$ and CO and, therefore, the remaining current not corresponding to the H$_2$ production would correspond to CO.

The reference electrode used for these experiments was a leakless AglAgCl (Innovative Instruments), calibrated against the reversible H$_2$ electrode by saturating the 0.1 M KHCO$_3$ electrolyte with H$_2$ and using Pt wires as the working and counter electrodes, respectively.

Tapping-Mode AFM. AFM measurements were carried out directly on the GC substrates as well as directly on the TEM grids using a Bruker Dimension Icon-Pt AFM in the tapping mode (TappingMode in Air, Steps non HAR) using the tip: Tap150Al-G silicon probe with aluminum reflex coating, resonant frequency 150k Hz, force constant 5 N/m, tip radius ∼10 nm. The heights of the NPs were measured by measuring individual line profiles and taking the height from a Gaussian fitting. The details of the data analysis in Gwyddion[42] and images for all NPs sizes are giving in Section S.2 in the Supporting Information.

SEM Imaging. SEM images were acquired using a Helios 5 Hydra UX PFIB SEM before and after electrochemistry, directly on the GC that were used for the electrochemical tests. All images were captured using the same physical parameters: accelerating voltage of 5 kV, and condenser lens strength current of 0.4 nA. We used two different detectors for each acquired image to reach more accurate conclusions about the size and composition of the sample, a secondary electron detector (TLD) and a backscatter detector (ABS). For each sample, several areas of the electrode were imaged to verify the homogeneity of the NP dispersion, and the size distribution is a combination of all these areas. Details on the image analysis done in ImageJ to extract the size distribution are given in Figure S5 in the Supporting Information. Post electrochemical SEM imaging is also provided in the Supporting Information, Section S.12. Sample extraction from the electrochemical cell, including the lost potential control, caused random influences on the sample surface, which meant that it was not possible post-mortem to obtain reproducible, accurate, and representative SEM images that reflected the catalyst in its working state.

HRTEM Measurements. Three samples prepared with differently sized NPs were deposited on commercial Au-covered Cu grids overlaid with Quantifoil and a suspended monolayer of graphene grown by chemical vapor deposition (Agar Scientific Ltd.). HRTEM images were acquired using a FEI Titan 80-300 Environmental Transmission Electron Microscope[43] equipped with a CEOS spherical aberration corrector for the objective lens in the TEM mode and operated at 300 keV primary beam energy in the HRTEM mode. Prior to imaging, the aberration corrector was tuned to an isotropic information transfer up to a scattering angle of 18 mrad and with the spherical aberration (C$_s$) coefficient set to 395 nm. All images were recorded using a Gatan K3 IS camera operated in the counting mode, using a low dose rate of 50 e$^-$/(Å^2·s), an exposure time of 4 s, and a pixel size of 0.218 Å/pixel. The beam was blanked in between successive images to limit accumulated dose exposure. Consecutive images revealed no observable change in the shape of the particles.

This fact together with the low applied dose rate suggests that beam-induced morphological changes of the samples NPs were suppressed.

Structure Modeling and Image Simulation. NP structure models were created in the Python-based atomic simulation environment (ASE)[44] using the package WulffPack.[45] Using the deposited masses from the cluster source divided by the mass of an Au atom, the number of Au atoms in each NP of diameter 1.5, 3.5, and 6.5 nm was estimated. The estimated number of atoms for each size, was used to create models of the NPs with particle sizes of a chosen number of atoms closest to 100 atoms (1.5 nm), 1320 atoms (3.5 nm), and 8500 atoms (6.5 nm) in the experimentally observed shapes (single crystal, icosahedral, and decahedral). Built-in ASE functions were utilized to evaluate the coordination number of each atom in the model. HRTEM images were simulated using the multislice approach implemented in the abTEM[46] Python environment. To mimic the FEI Titan 80−300 ETEM, the simulations were carried out with a primary beam energy of 300 keV, a spherical aberration coefficient of $C_s = 395$ nm, a pixel size of 0.218 Å/pixel, and a focal spread of 4.6 nm. Further, a slice thickness of 0.5 Å and a defocus value of −20 nm were used. Finally, to simulate realistic images, Poisson noise was also added to mimic shot noise. Shot noise is applicable since this is the dominating noise term when using the Gatan K3 IS. The shot noise was added using a built-in Python function in abTEM, taking the total dose used to capture each image $(200\ e^-/Å^2)$ as input.

■ ASSOCIATED CONTENT

ⓈⒾ Supporting Information

The Supporting Information is available free of charge at https://pubs.acs.org/doi/10.1021/jacs.3c10610.

> Additional experimental methods, further calibration and data analysis details, and supporting microscopy and spectroscopy information (PDF)

■ AUTHOR INFORMATION

Corresponding Author

Jakob Kibsgaard − *Department of Physics, Technical University of Denmark, 2800 Kongens Lyngby, Denmark; Center for Visualizing Catalytic Processes (VISION), Department of Physics, Technical University of Denmark, 2800 Kongens Lyngby, Denmark;* ⓞ orcid.org/0000-0002-9219-816X; Email: jkib@fysik.dtu.dk

Authors

Esperanza Sedano Varo − *Department of Physics, Technical University of Denmark, 2800 Kongens Lyngby, Denmark;* ⓞ orcid.org/0000-0002-3451-024X

Rikke Egeberg Tankard − *Department of Physics, Technical University of Denmark, 2800 Kongens Lyngby, Denmark;* ⓞ orcid.org/0000-0002-0060-642X

Joakim Kryger-Baggesen − *Center for Visualizing Catalytic Processes (VISION), Department of Physics, Technical University of Denmark, 2800 Kongens Lyngby, Denmark;* ⓞ orcid.org/0000-0002-7959-3309

Joerg Jinschek − *Center for Visualizing Catalytic Processes (VISION), Department of Physics and National Centre for Nano Fabrication and Characterization, Technical University of Denmark, 2800 Kongens Lyngby, Denmark*

Stig Helveg − *Center for Visualizing Catalytic Processes (VISION), Department of Physics, Technical University of Denmark, 2800 Kongens Lyngby, Denmark;* ⓞ orcid.org/0000-0002-0328-8295

Ib Chorkendorff − *Department of Physics, Technical University of Denmark, 2800 Kongens Lyngby, Denmark*

Christian Danvad Damsgaard − *Department of Physics, Technical University of Denmark, 2800 Kongens Lyngby, Denmark; Center for Visualizing Catalytic Processes (VISION), Department of Physics and National Centre for Nano Fabrication and Characterization, Technical University of Denmark, 2800 Kongens Lyngby, Denmark;* ⓞ orcid.org/0000-0002-3117-8616

Complete contact information is available at:
https://pubs.acs.org/10.1021/jacs.3c10610

■ REFERENCES

(1) *Research Needs towards Sustainable Production of Fuels and Chemicals*; Nørskov, J. K., Latimer, A.; Dickens, C. F., Eds., 2019. https://www.energy-x.eu/research-needs-report/.

(2) *Paris Agreement to the United Nations Framework Convention on Climate Change*, 2015.

(3) Kleis, J.; Greeley, J.; Romero, N. A.; Morozov, V. A.; Falsig, H.; Larsen, A. H.; Lu, J. J.; Mortensen, J. J.; Dułak, M.; Thygesen, K. S.; et al. Finite Size Effects in Chemical Bonding: From Small Clusters to Solids. *Catal. Lett.* **2011**, *141*, 1067−1071.

(4) Ishida, T.; Murayama, T.; Taketoshi, A.; Haruta, M. Importance of Size and Contact Structure of Gold Nanoparticles for the Genesis of Unique Catalytic Processes. *Chem. Rev.* **2020**, *120*, 464−525.

(5) Tyo, E. C.; Vajda, S. Catalysis by clusters with precise numbers of atoms. *Nat. Nanotechnol.* **2015**, *10*, 577−588.

(6) Kleijn, S. E. F.; Lai, S. C. S.; Koper, M. T. M.; Unwin, P. R. Electrochemistry of Nanoparticles. *Angew. Chem., Int. Ed.* **2014**, *53*, 3558−3586.

(7) Bard, A. J. Inner-Sphere Heterogeneous Electrode Reactions. Electrocatalysis and Photocatalysis: The Challenge. *J. Am. Chem. Soc.* **2010**, *132*, 7559−7567.

(8) Johánek, V.; Laurin, M.; Grant, A. W.; Kasemo, B.; Henry, C. R.; Libuda, J. Fluctuations and Bistabilities on Catalyst Nanoparticles. *Science* **2004**, *304*, 1639−1644.

(9) Chen, M. S.; Goodman, D. W. Structure-activity relationships in supported Au catalysts. *Catal. Today* **2006**, *111*, 22−33.

(10) Zhu, W.; Michalsky, R.; Metin, Ö.; Lv, H.; Guo, S.; Wright, C. J.; Sun, X.; Peterson, A. A.; Sun, S. Monodisperse Au Nanoparticles for Selective Electrocatalytic Reduction of CO2 to CO. *J. Am. Chem. Soc.* **2013**, *135*, 16833−16836.

(11) Mistry, H.; Reske, R.; Zeng, Z.; Zhao, Z. J.; Greeley, J.; Strasser, P.; Cuenya, B. R. Exceptional Size-Dependent Activity Enhancement in the Electroreduction of CO 2 over Au Nanoparticles. *J. Am. Chem. Soc.* **2014**, *136*, 16473−16476.

(12) Patil, A. N.; Paithankar, D. Y.; Otsuka, N.; Andres, R. P. The minimum-energy structure of nanometer-scale gold clusters. *Z. Phys. D* **1993**, *26*, 135−137.

(13) Rahm, J. M.; Erhart, P. Beyond Magic Numbers: Atomic Scale Equilibrium Nanoparticle Shapes for Any Size. *Nano Lett.* **2017**, *17*, 5775−5781.

(14) Von Issendorff, B.; Palmer, R. E. A new high transmission infinite range mass selector for cluster and nanoparticle beams. *Rev. Sci. Instrum.* **1999**, *70*, 4497−4501.

(15) Trimarco, D. B.; Scott, S. B.; Thilsted, A. H.; Pan, J. Y.; Pedersen, T.; Hansen, O.; Chorkendorff, I.; Vesborg, P. C. Enabling real-time detection of electrochemical desorption phenomena with sub-monolayer sensitivity. *Electrochim. Acta* **2018**, *268*, 520−530.

(16) Valden, M.; Pak, S.; Lai, X.; Goodman, D. W. Structure sensitivity of CO oxidation over model Au/TiO2 catalysts. *Catal. Lett.* **1998**, *56*, 7−10.

(17) Mori, T.; Hegmann, T. Determining the composition of gold nanoparticles: a compilation of shapes, sizes, and calculations using geometric considerations. *J. Nanopart. Res.* **2016**, *18*, 295.

(18) Klapetek, P.; Valtr, M.; Nečas, D.; Salyk, O.; Dzik, P. Atomic force microscopy analysis of nanoparticles in non-ideal conditions. *Nanoscale Res. Lett.* **2011**, *6*, 514.

(19) Brandsch, R.; Bar, G.; Whangbo, M.-H. On the Factors Affecting the Contrast of Height and Phase Images in Tapping Mode Atomic Force Microscopy. *Langmuir* **1997**, *13*, 6349−6353.

(20) Gao, D.; Arán-Ais, R. M.; Jeon, H. S.; Roldan Cuenya, B. Rational catalyst and electrolyte design for CO2 electroreduction towards multicarbon products. *Nat. Catal.* **2019**, *2*, 198−210.

(21) Mistry, H.; Behafarid, F.; Reske, R.; Varela, A. S.; Strasser, P.; Roldan Cuenya, B. Tuning Catalytic Selectivity at the Mesoscale via Interparticle Interactions. *ACS Catal.* **2016**, *6*, 1075−1080.

(22) Marcandalli, G.; Monteiro, M. C. O.; Goyal, A.; Koper, M. T. M. Electrolyte Effects on CO2 Electrochemical Reduction to CO. *Acc. Chem. Res.* **2022**, *55*, 1900−1911.

(23) Marcandalli, G.; Goyal, A.; Koper, M. T. M. Electrolyte Effects on the Faradaic Efficiency of CO2 Reduction to CO on a Gold Electrode. *ACS Catal.* **2021**, *11*, 4936−4945.

(24) Ino, S. Epitaxial Growth of Metals on Rocksalt Faces Cleaved in Vacuum. II. Orientation and Structure of Gold Particles Formed in Ultrahigh Vacuum. *J. Phys. Soc. Jpn.* **1966**, *21*, 346−362.

(25) Wulff, G. XXV. Zur Frage der Geschwindigkeit des Wachsthums und der Auflösung der Krystallflächen. *Zeitschrift für Kristallographie - Crystalline Materials* **1901**, *34*, 449−530.

(26) Marks, L. D. Modified Wulff constructions for twinned particles. *J. Cryst. Growth* **1983**, *61*, 556−566.

(27) Tran, R.; Xu, Z.; Radhakrishnan, B.; Winston, D.; Sun, W.; Persson, K. A.; Ong, S. P. Surface energies of elemental crystals. *Sci. Data* **2016**, *3*, 160080.

(28) Suzuki, H.; Barrett, C. S. Deformation twinning in silver-gold alloys. *Acta Metall.* **1958**, *6*, 156−165.

(29) Feng, X.; Jiang, K.; Fan, S.; Kanan, M. W. Grain-Boundary-Dependent CO2 Electroreduction Activity. *J. Am. Chem. Soc.* **2015**, *137*, 4606−4609.

(30) Hu, K.-J.; Plant, S. R.; Ellis, P. R.; Brown, C. M.; Bishop, P. T.; Palmer, R. E. Atomic Resolution Observation of a Size-Dependent Change in the Ripening Modes of Mass-Selected Au Nanoclusters Involved in CO Oxidation. *J. Am. Chem. Soc.* **2015**, *137*, 15161−15168.

(31) Wells, D. M.; Rossi, G.; Ferrando, R.; Palmer, R. E. Metastability of the atomic structures of size-selected gold nanoparticles. *Nanoscale* **2015**, *7*, 6498−6503.

(32) Ohyama, J.; Koketsu, T.; Yamamoto, Y.; Arai, S.; Satsuma, A. Preparation of TiO2-supported twinned gold nanoparticles by CO treatment and their CO oxidation activity. *Chem. Commun.* **2015**, *51*, 15823−15826.

(33) Haruta, M. Size- and support-dependency in the catalysis of gold. *Catal. Today* **1997**, *36*, 153−166.

(34) Haruta, M.; Tsubota, S.; Kobayashi, T.; Kageyama, H.; Genet, M.; Delmon, B. Low-Temperature Oxidation of CO over Gold Supported on TiO2, α-Fe2O3, and Co3O4. *J. Catal.* **1993**, *144*, 175−192.

(35) Valden, M.; Lai, X.; Goodman, D. W. Onset of catalytic activity of gold clusters on titania with the appearance of nonmetallic properties. *Science* **1998**, *281*, 1647−1650.

(36) Falsig, H.; Hvolbæk, B.; Kristensen, I.; Jiang, T.; Bligaard, T.; Christensen, C.; Nørskov, J. Trends in the Catalytic CO Oxidation Activity of Nanoparticles. *Angew. Chem., Int. Ed.* **2008**, *47*, 4835−4839.

(37) Pratontep, S.; Carroll, S. J.; Xirouchaki, C.; Streun, M.; Palmer, R. E. Size-selected cluster beam source based on radio frequency magnetron plasma sputtering and gas condensation. *Rev. Sci. Instrum.* **2005**, *76*, 045103.

(38) Bernhardt, T. M.; Heiz, U.; Landman, U. "Chemical and Catalytic Properties of Size-Selected Free and Supported Clusters". *Nanocatalysis*; Heiz, U., Landman, U., Eds.; Springer: Berlin, 2007; pp 1−191.

(39) Scott, S. *GitHub—ixdat/ixdat: The In-situ Experimental Data Tool*, 2023.

(40) Hochfilzer, D.; Sørensen, J. E.; Clark, E. L.; Scott, S. B.; Chorkendorff, I.; Kibsgaard, J. The Importance of Potential Control for Accurate Studies of Electrochemical CO Reduction. *ACS Energy Lett.* **2021**, *6*, 1879−1885.

(41) Scott, S. Isotope-Labeling Studies in Electrocatalysis for Renewable Energy Conversion. Ph.D. Thesis, Technical University of Denmark, 2019.

(42) Nečas, D.; Klapetek, P. Gwyddion: an open-source software for SPM data analysis. *centr.eur.j.phys.* **2012**, *10*, 181−188.

(43) Jinschek, J. R.; Helveg, S. Image resolution and sensitivity in an environmental transmission electron microscope. *Micron* **2012**, *43*, 1156−1168.

(44) Hjorth Larsen, A.; Jørgen Mortensen, J.; Blomqvist, J.; Castelli, I. E.; Christensen, R.; Dułak, M.; Friis, J.; Groves, M. N.; Hammer, B.; Hargus, C.; et al. The atomic simulation environment—a Python library for working with atoms. *J. Phys.: Condens. Matter* **2017**, *29*, 273002.

(45) Rahm, J. M.; Erhart, P. WulffPack: A Python package for Wulff constructions. *J. Open Source Softw.* **2020**, *5*, 1944.

(46) Madsen, J.; Susi, T. abTEM: ab Initio Transmission Electron Microscopy Image Simulation. *Microsc. Microanal.* **2020**, *26*, 448−450.